Journal of
Materials Chemistry A

PAPER

View Article Online
View Journal | View Issue

Cite this: *J. Mater. Chem. A*, 2016, **4**, 9653

Facile synthesis of hierarchical MoS_2–carbon microspheres as a robust anode for lithium ion batteries†

Gen Chen,‡[a] Shengping Wang,‡[bc] Ran Yi,[d] Longfei Tan,[b] Hongbo Li,*[e] Meng Zhou,[a] Litao Yan,[a] Yingbing Jiang,[f] Shuai Tan,[g] Donghai Wang,[d] Shuguang Deng,[a] Xianwei Meng*[b] and Hongmei Luo*[a]

Received 20th April 2016
Accepted 24th May 2016

DOI: 10.1039/c6ta03310e

www.rsc.org/MaterialsA

Molybdenum disulfide (MoS_2) may be a promising alternative for lithium ion batteries (LIBs) because it offers a unique layered crystal structure with a large and tunable distance between layers. This enables the anticipated excellent rate and cycling stability because they can promote the reversible lithium ion intercalation and de-intercalation without huge volume change which consequently prevents the pulverization of active materials during repeated charge and discharge processes. Herein, we prepared hierarchical MoS_2–carbon (MoS_2–C) microspheres *via* a continuous and scalable ultrasonic nebulization assisted route. The structure, composition, and electrochemical properties are investigated in detail. The MoS_2–C microspheres consist of few-layer MoS_2 nanosheets bridged by carbon, which separates the exfoliated MoS_2 layers and prevents their aggregation and restacking, thus leading to improved kinetic, enhanced conductivity and structural integrity. The novel architecture offers additional merits such as overall large size and high packing density, which promotes their practical applications. The MoS_2–C microspheres have been demonstrated with excellent electrochemical performances in terms of low resistance, high capacity even at large current density, stable cycling performance, *etc.* The electrodes exhibited 800 mA h g^{-1} at 1000 mA g^{-1} over 170 cycles. At a higher current density of 3200 mA g^{-1}, a capacity of 730 mA h g^{-1} can be also maintained. The MoS_2–C microspheres are practically applicable not only because of the continuous and large scale synthesis *via* the current strategy, but also the possess a robust and integrated architecture which ensures the excellent electrochemical properties.

1. Introduction

Surging clean energy demands and great market potential have been continuously promoting the development of electrochemical energy storage (EES). Lithium ion batteries (LIBs) are one of the most important EES devices and have been widely applied in portable electronics and at the same time are receiving increasing attention as the dominant power supply for electric vehicles.[1–4] LIB performance, including cycling and rate capacity, stability, *etc.*, heavily depends on the properties of anode materials such as the theoretical specific capacity, electronic conductivity and reversibility. The exploration of new anode materials lies at the center of the development of advanced LIBs.[5–7] However, there are many barriers accompanying the utilization of new materials. For instance, Si delivers a high theoretical capacity over ∼4000 mA h g^{-1}, but the huge volume change of ∼400% (ref. 8 and 9) leads to lattice stress and consequently the deterioration of the structure of the electrode during charge and discharge (lithiation/delithiation) processes. Transition metal oxides or sulfides[10–14] are promising electrode materials with advantages such as low cost, easy synthesis and environmental friendliness. Unfortunately, these compounds

---

[a] *Department of Chemical and Materials Engineering, New Mexico State University, Las Cruces, New Mexico 88003, USA. E-mail: hluo@nmsu.edu*

[b] *Laboratory of Controllable Preparation and Application of Nanomaterials, Center for Micro/nanomaterials and Technology & Key Laboratory of Photochemical Conversion and Optoelectronic Materials, Technical Institute of Physics and Chemistry, Chinese Academy of Sciences, Beijing 100190, China. E-mail: mengxw@mail.ipc.ac.cn*

[c] *Department of Materials Science and Engineering, Jinan University, Guangzhou 510632, China*

[d] *Department of Nuclear and Mechanical Engineering, The Pennsylvania State University, University Park, Pennsylvania 16802, USA*

[e] *Beijing Key Laboratory of Construction-Tailorable Advanced Functional Materials and Green Applications, School of Materials Science & Engineering, Beijing Institute of Technology, Beijing 100081, China. E-mail: hbli@mail.ipc.ac.cn*

[f] *Center for Micro-Engineered Materials, University of New Mexico, Albuquerque, New Mexico 87131, USA*

[g] *School of Chemical & Biomolecular Engineering, Georgia Institute of Technology, Atlanta, Georgia 30332, USA*

† Electronic supplementary information (ESI) available: Schematic illustration of the synthetic process; size distribution, EDS spectra. See DOI: 10.1039/c6ta03310e

‡ These authors contributed equally to this work.

normally suffer from poor conductivity, solubility into the electrolyte, aggregation, *etc.*, and their commercial availability is thus greatly restricted.

Molybdenum disulfide (MoS_2) delivers a theoretical lithium ion capacity of 670 mA h g^{-1} and has been extensively investigated for electrochemical energy storage because of its unique layered crystal structure, featuring Mo atoms sandwiched between two layers of closely packed S atoms, linking the MoS_2 layers by a weak van der Waals interaction.[15–17] The large and tunable distance between adjacent layers enables the anticipated excellent rate and cycling stability because they can promote the reversible lithium ion intercalation and de-intercalation without a huge volume change and consequently prevent the pulverization of active materials during repeated charge and discharge processes. However, bulk or nanoscale MoS_2 suffers from poor conductivity for electron/ion transfer, which is responsible for severe capacity loss after a few cycles. Moreover, the MoS_2-based electrodes provide high capacity through similar electrochemical redox reactions with lithium sulfide batteries in essence, which may also lead to their degradation by the polysulfide shuttling effect.[18,19]

To overcome these barriers, numerous efforts have been directed towards rational design and fabrication of MoS_2 nanostructures with optimized electrochemical performance compared to their bulk counterparts.[20–27] One effective strategy is to make MoS_2 into a few expanded layers, which provides a larger surface area, shorter lithium ion diffusion path and thus improved kinetics. Hierarchical MoS_2 microspheres[28] or microboxes[29,30] composed of few-layered nanosheets are therefore developed with enhanced electrochemical properties for lithium storage. In addition, supporting carbon materials show great potential for electrochemical energy storage applications[31–33] because they exhibit several interesting properties, including high electrical conductivity, excellent stability, large surface area and tunable porous structure. Up to date, a variety of carbon-based materials such as graphene,[34–36] CNTs,[37] porous carbon,[38] *etc.*, have been widely applied as either supporting or conducting agent in electrodes for much improved electrochemical performance in terms of stability and capacity. The development of advanced composite materials built of well-controlled nanostructured MoS_2 and carbon has also been a very active research topic.[39–44] Combining conductive carbon with MoS_2 has been proved to enhance the electron transport, cycling stability and structural integrity during the lithium ion insertion/extraction processes. Most recently, a new two-dimensional MoS_2 with a chemically synthesized mesoporous carbon hybrid nanoarchitecture was designed for LIBs, with an ideal MoS_2/mesoporous carbon atomic interface in which single layer MoS_2 and mesoporous carbon are sandwiched in an alternating sequence.[45] The nanoarchitecture showed excellent electrochemical performance, indicating the unbeatable advantages of nanoscale engineering.

Nevertheless, complicated procedures are frequently involved in the synthesis of these nanoarchitectures, which are not practically applicable for continuous and large scale production. Herein, we prepared unique hierarchical MoS_2–carbon (MoS_2–C) microspheres *via* a facile continuous and scalable ultrasonic nebulization route. The hierarchical MoS_2–C microspheres consist of few-layer MoS_2 nanosheets bridged by carbon, which separates the exfoliated MoS_2 layers and prevents their aggregation and restacking. The novel architecture offers additional merits such as overall large size and high packing density, which promote their practical applications. The as-prepared MoS_2–C microspheres demonstrate excellent electrochemical performance in terms of low resistance, high capacity even at large current density, stable cycling capacity, *etc.* Specifically, the electrodes exhibited around 800 mA h g^{-1} at 1000 mA g^{-1} over long cycles. At a higher current density of 3200 mA g^{-1}, a capacity of 730 mA h g^{-1} can be maintained. The MoS_2–C microspheres are of practical potential because of not only the continuous and large scale synthesis *via* the current strategy, but also the robust and integrated architecture which ensures excellent electrochemical properties.

2. Experimental section

Synthesis of hierarchical MoS_2–C microspheres

The MoS_2–C microspheres were synthesized by a continuous and scalable ultrasonic nebulization method (Fig. S1†). The precursor solution was prepared by adding 0.3 g $Na_2MoO_4\cdot 2H_2O$, 0.4 g $(NH_2)_2CS$ and 0.3 g citric acid into a bottle with 30 ml distilled water. Then the pH of the solution was adjusted to 3. After the solution was nebulized *via* an ultrasonic nebulization device, the droplets were formed and carried into a tube furnace (600 °C) by a continuous flow of argon. The annealed products were collected in a sample collector. By washing with distilled water and centrifuging at 12 000 rpm for 8 min, MoS_2–C microspheres were obtained after the removal of residual acid and precursors from annealed products.

Characterization

The phase and structure of the obtained products were determined on a Rigaku MiniFlex II X-ray powder diffractometer with Cu Kα radiation ($\lambda = 1.5418$ Å). The operation voltage and current were kept at 40 kV and 30 mA, respectively. The size, morphology and lattice parameters were determined by transmission electron microscopy (TEM, JEOL JEM 2010) operating at an accelerating voltage of 200 kV; scanning transmission electron microscopy (STEM, JEOL 2010 FEG TEM STEM with Oxford EDS) and scanning electron microscopy (SEM, Models 4300 and 4800, Hitachi). Energy-dispersive X-ray spectroscopy and elemental mapping were taken on transmission electron microscope. Raman spectra were collected using a Reinshaw Raman microscope with 632.8 nm (1.96 eV) laser excitation. Fourier transform infra-red (FTIR) spectroscopy was obtained on a Bruker Vertex 80v optical bench. The Brunauer–Emmett–Teller (BET) surface area was recorded by a Micromeritics ASAP 2020 using standard N_2 adsorption and desorption isotherm measurements at 77 K. Thermogravimetric analysis (TGA, Perkin-Elmer Pyris 1) was carried out in the temperature range 25–700 °C at a heating rate of 10 °C min^{-1} in air and X-ray photoelectron spectroscopy (XPS) was recorded using a Thermo K-Alpha spectrometer equipped with a monochromatic Al Kα X-ray source.

Electrochemical test

The electrochemical performance was evaluated by galvanostatic charge/discharge cycling on a LAND CT2001A multichannel battery testing system at room temperature using 2032-type coin cells, which were assembled in an argon-filled dry glovebox (Vigor Gas Purification Technologies, Inc.) with trace amounts of oxygen and moisture below 1 ppm. The working electrodes were prepared by casting the slurry (80 wt% of active material, 10 wt% of carbon black, and 10 wt% of polyacrylic acid binder) on nickel foam (MTI). The electrode loading amount was around 3.0 mg. The counter electrode was made of lithium metal. The electrolyte was composed of 1 M $LiPF_6$ in a mixture of ethylene carbonate and dimethyl carbonate (1 : 1 by volume). Specific capacity is calculated based on the mass of active material. Cyclic voltammetry curves of the prepared coin cells were obtained on a VersaSTAT 4 with a scan rate of 0.2 mV s^{-1}. The electrochemical impedance spectroscopy of fresh coin cells and coin cells after cycling was recorded on a CHI-680A (CH Instruments, Inc) electrochemical workstation using zero bias potential.

3. Results and discussion

The shape and morphology of the hierarchical MoS_2–C microspheres were firstly characterized by scanning electron microscopy (SEM) and transmission electron microscopy (TEM) as shown in Fig. 1. The MoS_2–C microspheres display a wide size distribution from several hundred nanometers to microns with well-defined spherical shape (Fig. 1a and S2†), which is attributed to the droplets formed with random sizes. A close TEM shot (Fig. 1b and c) on a single sphere reveals the nature of assembly of these microspheres by MoS_2 nanosheets. We deduce that the greyish area between MoS_2 nanosheets is filled with amorphous carbon, which is further interpreted in the following part. The high resolution TEM results (Fig. 1d) further confirm the layered structure of MoS_2 nanosheets with a distance of 0.64 nm between adjacent layers, corresponding to the (002) lattice plane. The slightly enlarged layer spacing indicates the less ordered structure and confinement of MoS_2 nanosheets compared with their bulk counterpart, which may facilitate the insertion of lithium ions during electrochemical reaction and therefore ensures the deep utilization of active materials. Another group of clear lattice fringes corresponding to the (100) plane can also be observed with a distance of 0.27 nm. As shown in Fig. 1e, the fast Fourier transform (FFT) derived from Fig. 1d shows two dominant crystal planes of (002) and (100) and their crystal structure schemes are presented in Fig. 1f, corresponding to the viewpoint from the *b* and *c* axes, respectively. The layered crystal structure of MoS_2 can be generally described as Mo atoms sandwiched between two layers of closely packed S atoms and the MoS_2 layers are linked by a weak van der Waals interaction, leading to a large and tunable distance between layers. Dark field STEM images with different magnifications present the contrast between Mo and C, indicating blurry carbon distributed homogeneously among the MoS_2 nanosheets (Fig. 1g and S3†). The elemental maps

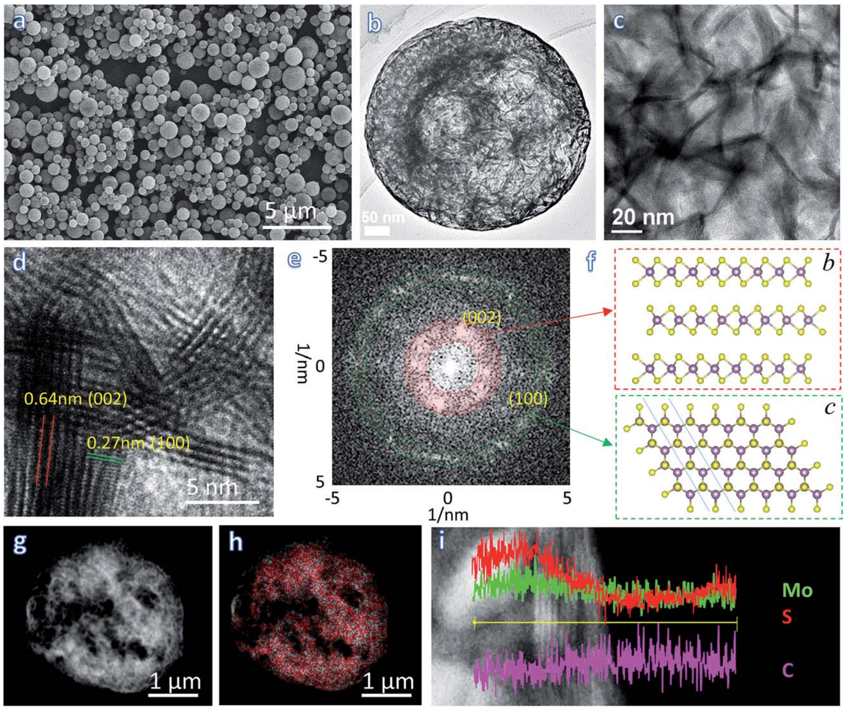

Fig. 1 Morphological and structural characterizations. (a) SEM image; (b, c) close shot of a single sphere and detailed microstructure observed by TEM; (d) high resolution TEM image and (e) corresponding FFT pattern; (f) crystal structure observed from *b* and *c* axes, corresponding to the two rings in (e); (g) STEM image of a single microsphere; (h) over-lapped elemental maps of Mo, S taken using STEM and (i) elemental linescans of Mo, S and C at high magnification.

taken using STEM again demonstrate that the Mo and S are distributed uniformly along the nanosheets (Fig. 1h). The ratio of Mo : S is determined to be 1 : 2 as shown in Fig. S4,† which agrees with the stoichiometry of MoS_2. The elemental line-scan obtained at high magnification further discloses the distribution of different elements along the selected region (Fig. 1i). The signals of Mo, S, and C decrease geometrically towards the surface of microsphere.

The crystallinity of the as-prepared hierarchical MoS_2–C microspheres was revealed by X-ray diffraction (XRD) as shown in Fig. 2a. All of the identified peaks can be readily assigned to the standard hexagonal MoS_2 (JCPDS 37-1492). The obvious broadness of all the peaks in the XRD pattern indicates the nanoscale crystallites, which is consistent with the TEM observation. It is noteworthy that the 2θ of the (002) diffraction peak was shifted to a lower angle, corresponding to an increased interlayer distance of the (002) plane. The limited number of S–Mo–S layers also led to clear differences shown using Raman spectroscopy, which has been applied as a reliable diagnostic technique to investigate the ultrathin nature of MoS_2 nanosheets. Fig. 2b shows the typical Raman spectra of the hierarchical MoS_2–C microspheres and bulk MoS_2 materials excited with a 532 nm laser at room temperature. The insets illustrate two typical vibrations of the S–Mo–S interaction and movement, in which the in-plane E^1_{2g} mode can be assigned to an opposite vibration of the Mo atom with respect to two S atoms, and the A_{1g} mode is ascribed to the out-of-plane vibration of S atoms along opposite directions.[15,46] A negligible shift can be seen for the frequency at about 380 cm^{-1}, indicating a similar in-plane vibration behavior of both MoS_2–C microspheres and bulk MoS_2. On the contrary, the A_{1g} peak shifts from 406.7 cm^{-1} for the bulk MoS_2 to 404.1 cm^{-1} for the hierarchical MoS_2–C microspheres. The few-layer nature leads to reduced interlayer van der Waals interactions and therefore results in an obviously increased out-of-plane atom vibration (A_{1g}) along the *c* axis which has a limited impact on the in-plane vibration (E^1_{2g}). A TGA technique was further applied to determine the amount of carbon in the composite. No obvious mass difference is presented up to 100 °C as shown in Fig. 2c. The formation of MoO_3 from MoS_2 and the combustion of carbon in O_2 flow occur in the same temperature range 300–400 °C, leading to the main loss of 23 wt%. The oxidation of MoS_2 is revealed by a small platform at 320 °C. By assuming that the final product after 400 °C is MoO_3, the weight fraction of carbon in the initial sample can be simply estimated to be about 15%. FTIR spectroscopy was carried out to investigate the detailed chemical bonding information in the composite (Fig. 2d). Characteristic peaks of carbon centered at 2913, 1630, 1412, 1140 and 1030 cm^{-1} can be assigned to different vibrations of C–H, C=C, COO^-, C–O and C–C, respectively.[47]

XPS of the hierarchical MoS_2–C microspheres was also carried out to analyze their composition. As shown in Fig. 3a, Mo, S, and C can be readily indexed in the XPS survey spectra. High-resolution XPS spectra of Mo (Fig. 3b) displays two characteristic peaks of Mo $3d_{3/2}$ and Mo $3d_{5/2}$ centered at 232.5 and 229.5 eV, respectively, which are assigned to Mo^{4+} in MoS_2.[15,29] A minor peak belonging to S 2s can also be observed next to Mo $3d_{5/2}$. The peaks located at 163.5 and 162.3 eV in the fine scan of

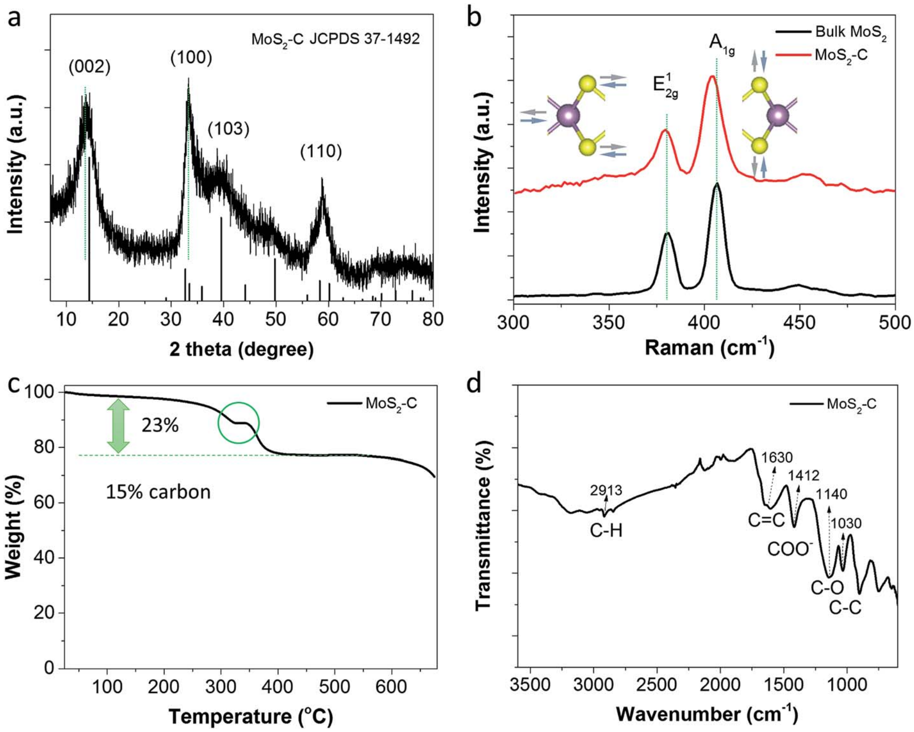

Fig. 2 (a) XRD pattern; (b) Raman spectra with insets indicating the two different vibration modes; (c) TGA profile and (d) FTIR spectra of the hierarchical MoS_2–C microspheres.

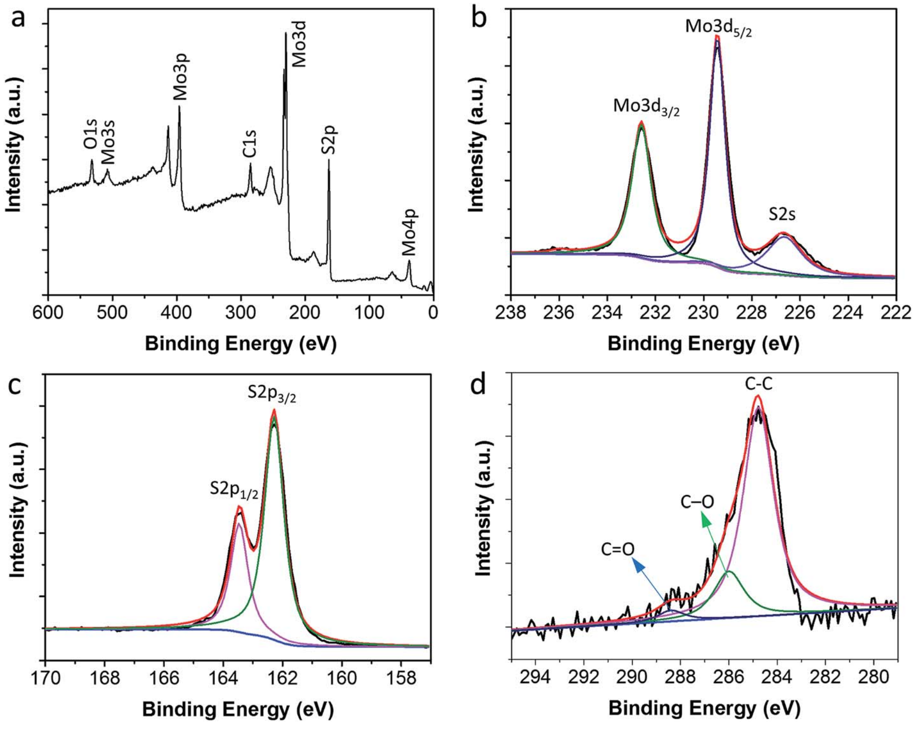

Fig. 3 (a) XPS survey spectrum of the hierarchical MoS_2–C microspheres and the corresponding high-resolution XPS scans of (b) Mo 3d, (c) S 2p and (d) C 1s.

S 2p (Fig. 3c) are attributed to the S $2p_{3/2}$ and S $2p_{1/2}$ components. A high-resolution spectrum of C 1s was also recorded as shown in Fig. 3d. Carbon species of C–C, C–O, C═O can be determined by fitting the XPS profile, which is in good agreement with the FTIR results, indicating the successful preparation of MoS_2–C composites.

Full N_2 adsorption–desorption isotherms on the hierarchical MoS_2–C microspheres were measured to reveal the pore size distribution and specific surface area of these microspheres. As shown in Fig. 4a, the isotherms of MoS_2–C microspheres display a quasi IV isotherm characteristic of mesoporous materials.[15,45,48] The Brunauer–Emmett–Teller specific surface area of MoS_2–C microspheres is determined to be 78 m^2 g^{-1}. The pore size distribution (Fig. 4b) calculated using the Barrett–Joyner–Halenda model shows two obvious peaks at 2.6 and 10.0 nm, respectively. The relatively large mesopores can be ascribed to mesoporous channels in the MoS_2–C microspheres resulting from a mutual crisscross space of the assembly and restacking hierarchical architecture. Meanwhile, the smaller mesopores may be attributed to the carbon itself. The novel architecture leaves plenty of space for accommodating the volumetric expansion during the lithiation process as well as channels for the mass transport, which are two critical factors for the enhancement of the power/energy density of LIBs.

The obtained nanoarchitecture featuring few-layer MoS_2 nanosheets bridged by mesoporous carbon has unique advantages as an anode material for LIBs: (1) separated MoS_2 nanosheets by carbon can prevent aggregation and restacking during

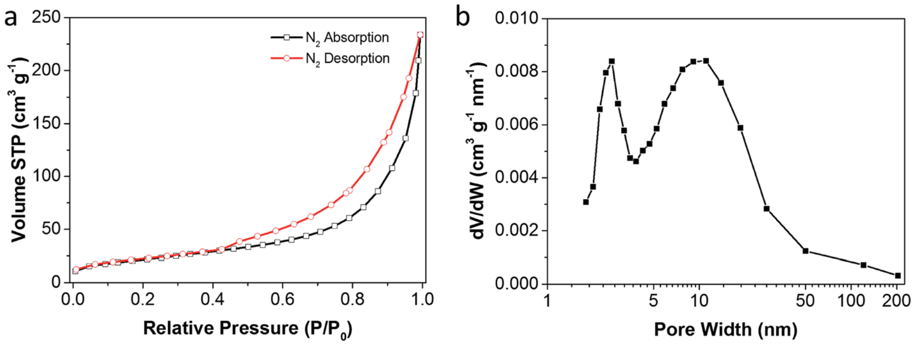

Fig. 4 (a) Nitrogen adsorption–desorption isotherms of the hierarchical MoS_2–C microspheres at 77 K; and (b) corresponding pore size distribution.

lithiation/delithiation and simultaneously improve the electronic conductivity; (2) void space can facilitate the mass transport and accommodate the volume change; (3) the microsize nature enables a higher packing density over nanoparticles. With these merits in mind, the electrochemical behavior of the MoS_2–C microspheres as anode materials for LIBs was investigated. The first five CV scans of the hierarchical MoS_2–C microspheres are displayed in Fig. 5a. Two clear reduction peaks centered at around 1.0 and 0.4 V in the first cathodic sweep can be observed. The peak (#1) at 1.0 V can be assigned to the insertion of Li^+ into MoS_2 interlayers to form Li_xMoS_2, leading to a phase transformation of MoS_2 from trigonal prismatic to octahedral structure.[49] The peak (#2) at 0.4 V may involve the further conversion reaction of MoS_2 ($MoS_2 + 4Li \rightarrow Mo + 2Li_2S$).[50,51] In the following four cathodic scans, different discharge profiles are obtained with two peaks at 1.9 V and 1.2 V, which can be attributed to the reduction of sulfur ($2Li^+ + S + 2e^- \rightarrow Li_2S$) and intercalation of Li^+ ($MoS_2 + xLi^+ + xe^- \rightarrow Li_xMoS_2$), respectively.[45,52–54] It is noteworthy that the insertion of Li^+ appears at higher voltage, indicating a quicker electrochemical response. The reduction peak current of sulfur is slightly increased with cycling, which may be due to an activation process of the electrode materials. In the reverse anodic sweep, we observe an obvious oxidation peak (#3) at 2.33 V, which is attributed to the delithiation of Li_2S ($Li_2S \rightarrow 2Li^+ + S + 2e^-$). Meanwhile, a broad and weak peak at 1.70 V can be seen, indicating the partial oxidation of metallic Mo.[52] A negligible peak shift related to the Li_2S/S reaction is observed, showing the good reversibility of hierarchical MoS_2–C microspheres. The first three charge and discharge profiles of the hierarchical MoS_2–C microspheres at a current density of 200 mA g^{-1} in the voltage range of 0.01 and 3.0 V are displayed in Fig. 5b. The initial discharge and charge capacities are determined to be 1200 mA h g^{-1} and 980 mA h g^{-1}, respectively. A corresponding coulombic efficiency of 81% is obtained and the irreversible capacity loss in the first cycle is mainly attributed to the formation of a solid electrolyte interface (SEI) layer.[52–54] The inflection voltage and platforms assigned to different electrochemical reactions are readily found, which are in good agreement with the CV results. The coulombic efficiency rapidly reaches ~97% in the second cycle and is maintained above 99.5% in the following cycles, indicating the efficient transport of electrons and reversible insertion/extraction of Li^+ in the hierarchical MoS_2–C microspheres. The stability of the hierarchical MoS_2–C microspheres was also investigated in terms of rate and cycling capability retention (Fig. 5c and d). The coin cells are subject to the rate capacity test at different current densities from 200 to 3200 mA g^{-1}. Typical ladder-like profiles can be observed and the corresponding discharge capacities of the hierarchical MoS_2–C microspheres are 917, 886, 855, 803, and 731 mA h g^{-1} at current densities of 200, 400, 800, 1600, and 3200 mA g^{-1}, respectively. By resetting the current density to 200 mA g^{-1}, the discharge capacity can be rebounded to about 990 mA h g^{-1}, indicating the robust nature of hierarchical MoS_2–C microspheres. Remarkably, the rate performance is superior over recently reported MoS_2 nanospheres,[15] nanoflowers[55] or nanosheets,[56] *etc.*, due to the favorable characteristics of the nanoarchitecture as anode materials.

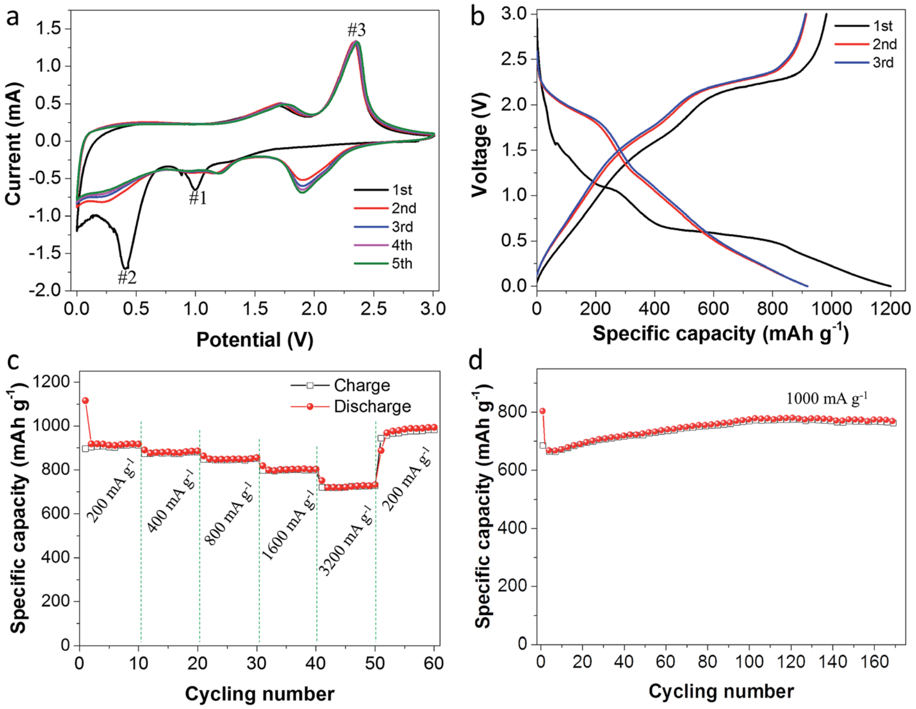

Fig. 5 Electrochemical performance of the hierarchical MoS_2–C microspheres. (a) CV scans for the initial five cycles at 0.2 mV s^{-1}; (b) charge/discharge curves for the first three cycles at 200 mA g^{-1}; (c) rate capacity at different current densities from 200 to 3200 mA g^{-1}; and (d) cycling performance of the hierarchical MoS_2–C microspheres at 1000 mA g^{-1}.

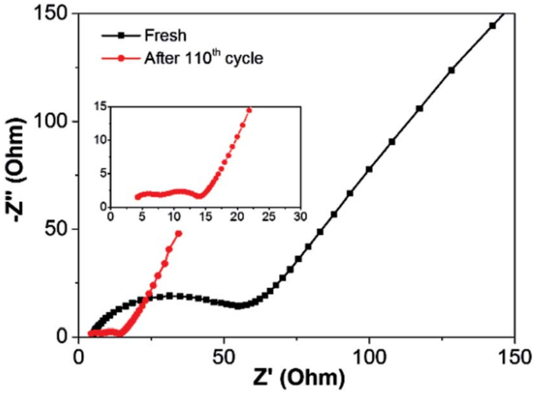

Fig. 6 EIS spectra of the hierarchical MoS_2–C microspheres before and after 110 charge and discharge cycles at 1000 mA g^{-1}.

To demonstrate the long cycling stability at a high current density, the hierarchical MoS_2–C microspheres are also tested at 1000 mA g^{-1}. It is found that the capacity eventually increases to 780 mA h g^{-1} at the 100th cycle at 1000 mA g^{-1}, which may be ascribed to the activation of electrode materials. The gravimetric energy density of the electrodes was calculated to be 2340 Wh kg^{-1}. The high coulombic efficiency of 85% is calculated for the initial cycle, indicating efficient and fast mass transport. It is believed that the introduction of carbon may change the SEI formation behavior by forming a stable SEI layer on the carbon instead of the transition metal compounds, which prevents the repeated cracking and formation processes.[57,58]

The electrochemical impedance spectroscopy (EIS) of the hierarchical MoS_2–C microspheres before and after 110 charge and discharge cycles (at 1000 mA g^{-1}) was evaluated, as shown in Fig. 6. The semicircle in the high-frequency region can be ascribed to the constant phase element of the SEI layer and contact resistance. The medium-frequency semicircle is related to charge-transfer impedance and the constant phase element of the electrode/electrolyte interface. The inclined line is attributed to Warburg impedance corresponding to the lithium-diffusion process. It is clearly observed that the diameter of semicircles is significantly decreased after cycling, which is in accordance with the activation process. The reduced resistance can facilitate the ionic and electronic transport in the composite, which is crucial for Li^+ insertion/extraction and therefore excellent electrochemical performance is observed.

4. Conclusions

In this work, hierarchical MoS_2–C microspheres have been successfully designed and fabricated by a facile and scalable ultrasonic nebulization route. The novel architecture consists of few-layer MoS_2 nanosheets bridged with mesoporous carbon, which offers several distinguished advantages that contribute to the excellent electrochemical performance. First, the assembly nature of hierarchical MoS_2–C microspheres ensures a relatively larger pack density over the hollow structures but leaves enough void space for fast mass transport, enhanced active material–electrolyte contact area and accommodated volumetric change during Li^+ insertion/desertion. Second, mesoporous carbon plays multiple roles in enhancing performance. It not only improves the conductivity and thus the charge transfer, but also restricts polysulfide shuttling of intermediate polysulfides resulting from the intrinsic sulfur reaction. Therefore, the MoS_2–C microspheres have delivered excellent electrochemical properties such as low resistance, high rate capacity, stable cycling capacity, *etc.* Specifically, the electrodes exhibited around 800 mA h g^{-1} at 1000 mA g^{-1} over long cycles. At higher current density of 3200 mA g^{-1}, a capacity of 730 mA h g^{-1} can be also maintained. The MoS_2–C microspheres are of practical potential not only because of the continuous and large scale synthesis *via* the current strategy, but also the robust and integrated architecture which ensures its excellent electrochemical properties. The current synthetic strategy can also be extended for the fabrication of other anode materials with heterostructured architectures for high performance LIBs.

Acknowledgements

G. C. greatly thanks the 2015 ECS Edward G. Weston Summer Fellowship and Chinese Government Award for Outstanding Self-Financed Students Abroad from China Scholarship Council. M. X. acknowledges the funding support from Beijing Natural Science Foundation (No. 4161003) and Youth Innovation Promotion Association of Chinese Academy of Sciences (2014023). H. L. acknowledges the partial funding support from the National Science Foundation DMR-1449035, the New Mexico EPSCoR with NSF-1301346, and Argonne National Laboratory. Argonne, a U.S. Department of Energy Office of Science laboratory, is operated under Contract No. DE-AC02-06CH11357.

References

1 J. B. Goodenough and K.-S. Park, *J. Am. Chem. Soc.*, 2013, **135**, 1167–1176.
2 M. M. Thackeray, C. Wolverton and E. D. Isaacs, *Energy Environ. Sci.*, 2012, **5**, 7854–7863.
3 S. Chu and A. Majumdar, *Nature*, 2012, **488**, 294–303.
4 N.-S. Choi, Z. Chen, S. A. Freunberger, X. Ji, Y.-K. Sun, K. Amine, G. Yushin, L. F. Nazar, J. Cho and P. G. Bruce, *Angew. Chem., Int. Ed.*, 2012, **51**, 9994–10024.
5 L. Li, Z. Wu, S. Yuan and X.-B. Zhang, *Energy Environ. Sci.*, 2014, **7**, 2101–2122.
6 P. Roy and S. K. Srivastava, *J. Mater. Chem. A*, 2015, **3**, 2454–2484.
7 X. Rui, H. Tan and Q. Yan, *Nanoscale*, 2014, **6**, 9889–9924.
8 X. Su, Q. Wu, J. Li, X. Xiao, A. Lott, W. Lu, B. W. Sheldon and J. Wu, *Adv. Energy Mater.*, 2014, **4**, 1300882.
9 J. R. Szczech and S. Jin, *Energy Environ. Sci.*, 2011, **4**, 56–72.
10 C. Tan and H. Zhang, *Chem. Soc. Rev.*, 2015, **44**, 2713–2731.
11 H. Wang, H. Yuan, S. Sae Hong, Y. Li and Y. Cui, *Chem. Soc. Rev.*, 2015, **44**, 2664–2680.
12 S. Dong, X. Chen, X. Zhang and G. Cui, *Coord. Chem. Rev.*, 2013, **257**, 1946–1956.

13 V. Augustyn, P. Simon and B. Dunn, *Energy Environ. Sci.*, 2014, **7**, 1597–1614.

14 C. Yuan, H. B. Wu, Y. Xie and X. W. Lou, *Angew. Chem., Int. Ed.*, 2014, **53**, 1488–1504.

15 S. Zhang, B. V. R. Chowdari, Z. Wen, J. Jin and J. Yang, *ACS Nano*, 2015, **9**, 12464–12472.

16 X. Chia, A. Y. S. Eng, A. Ambrosi, S. M. Tan and M. Pumera, *Chem. Rev.*, 2015, **115**, 11941–11966.

17 T. Stephenson, Z. Li, B. Olsen and D. Mitlin, *Energy Environ. Sci.*, 2014, **7**, 209–231.

18 X. Ji, K. T. Lee and L. F. Nazar, *Nat. Mater.*, 2009, **8**, 500–506.

19 Y. V. Mikhaylik and J. R. Akridge, *J. Electrochem. Soc.*, 2004, **151**, A1969–A1976.

20 L. R. Hu, Y. M. Ren, H. X. Yang and Q. Xu, *ACS Appl. Mater. Interfaces*, 2014, **6**, 14644–14652.

21 J. Shao, Q. Qu, Z. Wan, T. Gao, Z. Zuo and H. Zheng, *ACS Appl. Mater. Interfaces*, 2015, **7**, 22927–22934.

22 C. Y. Zhao, J. H. Kong, X. Y. Yao, X. S. Tang, Y. L. Dong, S. L. Phua and X. H. Lu, *ACS Appl. Mater. Interfaces*, 2014, **6**, 6392–6398.

23 X. Xu, Z. Fan, X. Yu, S. Ding, D. Yu and X. W. Lou, *Adv. Energy Mater.*, 2014, **4**, 1400902.

24 Z. Hu, L. X. Wang, K. Zhang, J. B. Wang, F. Y. Cheng, Z. L. Tao and J. Chen, *Angew. Chem., Int. Ed.*, 2014, **53**, 12794–12798.

25 D. B. Kong, H. Y. He, Q. Song, B. Wang, W. Lv, Q. H. Yang and L. J. Zhi, *Energy Environ. Sci.*, 2014, **7**, 3320–3325.

26 R. H. Wang, C. H. Xu, J. Sun, Y. Q. Liu, L. Gao, H. L. Yao and C. C. Lin, *Nano Energy*, 2014, **8**, 183–195.

27 W. H. Ryu, J. W. Jung, K. Park, S. J. Kim and I. D. Kim, *Nanoscale*, 2014, **6**, 10975–10981.

28 S. Ding, D. Zhang, J. S. Chen and X. W. Lou, *Nanoscale*, 2012, **4**, 95–98.

29 X.-Y. Yu, H. Hu, Y. Wang, H. Chen and X. W. Lou, *Angew. Chem., Int. Ed.*, 2015, **54**, 7395–7398.

30 Z. Zhang, J. Liu, J. Gu, L. Su and L. Cheng, *Energy Environ. Sci.*, 2014, **7**, 2535–2558.

31 S. L. Candelaria, Y. Shao, W. Zhou, X. Li, J. Xiao, J.-G. Zhang, Y. Wang, J. Liu, J. Li and G. Cao, *Nano Energy*, 2012, **1**, 195–220.

32 X. Wang, G. Li, Z. Chen, V. Augustyn, X. Ma, G. Wang, B. Dunn and Y. Lu, *Adv. Energy Mater.*, 2011, **1**, 1089–1093.

33 Z. Chen, Y. Yuan, H. Zhou, X. Wang, Z. Gan, F. Wang and Y. Lu, *Adv. Mater.*, 2014, **26**, 339–345.

34 S. Han, D. Wu, S. Li, F. Zhang and X. Feng, *Adv. Mater.*, 2014, **26**, 849–864.

35 H. Chang and H. Wu, *Energy Environ. Sci.*, 2013, **6**, 3483–3507.

36 Y. Sun, Q. Wu and G. Shi, *Energy Environ. Sci.*, 2011, **4**, 1113–1132.

37 B. J. Landi, M. J. Ganter, C. D. Cress, R. A. DiLeo and R. P. Raffaelle, *Energy Environ. Sci.*, 2009, **2**, 638–654.

38 T.-Y. Ma, L. Liu and Z.-Y. Yuan, *Chem. Soc. Rev.*, 2013, **42**, 3977–4003.

39 C. Zhu, X. Mu, P. A. van Aken, J. Maier and Y. Yu, *Adv. Energy Mater.*, 2015, **5**, 1401170.

40 S. H. Choi and Y. C. Kang, *ChemSusChem*, 2015, **8**, 2260–2267.

41 S. Hu, W. Chen, J. Zhou, F. Yin, E. Uchaker, Q. Zhang and G. Cao, *J. Mater. Chem. A*, 2014, **2**, 7862–7872.

42 Y. Wang, G. Z. Xing, Z. J. Han, Y. M. Shi, J. I. Wong, Z. X. Huang, K. Ostrikov and H. Y. Yang, *Nanoscale*, 2014, **6**, 8884–8890.

43 L. S. Zhang, W. Fan and T. X. Liu, *RSC Adv*, 2015, **5**, 43130–43140.

44 Z. M. Wan, J. Shao, J. J. Yun, H. Y. Zheng, T. Gao, M. Shen, Q. T. Qu and H. H. Zheng, *Small*, 2014, **10**, 4975–4981.

45 H. Jiang, D. Ren, H. Wang, Y. Hu, S. Guo, H. Yuan, P. Hu, L. Zhang and C. Li, *Adv. Mater.*, 2015, **27**, 3687–3695.

46 H. Li, Q. Zhang, C. C. R. Yap, B. K. Tay, T. H. T. Edwin, A. Olivier and D. Baillargeat, *Adv. Funct. Mater.*, 2012, **22**, 1385–1390.

47 L. Yan, G. Chen, S. Tan, M. Zhou, G. Zou, S. Deng, S. Smirnov and H. Luo, *ACS Appl. Mater. Interfaces*, 2015, **7**, 24212–24217.

48 S. Qin, W. Lei, D. Liu and Y. Chen, *Sci. Rep.*, 2014, **4**, 7582.

49 C. Zhu, X. Mu, P. A. van Aken, Y. Yu and J. Maier, *Angew. Chem., Int. Ed.*, 2014, **53**, 2152–2156.

50 Z. Wang, T. Chen, W. X. Chen, K. Chang, L. Ma, G. C. Huang, D. Y. Chen and J. Y. Lee, *J. Mater. Chem. A*, 2013, **1**, 2202–2210.

51 L. Fei, Y. Xu, X. F. Wu, G. Chen, Y. L. Li, B. S. Li, S. G. Deng, S. Smirnov, H. Y. Fan and H. M. Luo, *Nanoscale*, 2014, **6**, 3664–3669.

52 L. C. Yang, S. N. Wang, J. J. Mao, J. W. Deng, Q. S. Gao, Y. Tang and O. G. Schmidt, *Adv. Mater.*, 2013, **25**, 1180–1184.

53 K. Zhang, H. J. Kim, X. J. Shi, J. T. Lee, J. M. Choi, M. S. Song and J. H. Park, *Inorg. Chem.*, 2013, **52**, 9807–9812.

54 H. Li, X. Wang, B. Ding, G. Pang, P. Nie, L. Shen and X. Zhang, *ChemElectroChem*, 2014, **1**, 1118–1125.

55 T. Yang, Y. Chen, B. Qu, L. Mei, D. Lei, H. Zhang, Q. Li and T. Wang, *Electrochim. Acta*, 2014, **115**, 165–169.

56 S. K. Park, S. H. Yu, S. Woo, B. Quan, D. C. Lee, M. K. Kim, Y. E. Sung and Y. Piao, *Dalton Trans.*, 2013, **42**, 2399–2405.

57 Y. Li, K. Yan, H.-W. Lee, Z. Lu, N. Liu and Y. Cui, *Nat. Energy*, 2016, **1**, 15029.

58 J. Shin, W.-H. Ryu, K.-S. Park and I.-D. Kim, *ACS Nano*, 2013, **7**, 7330–7341.